Authors' accepted version. Engineering Fracture Mechanics, 112173 (2026).
https://doi.org/10.1016/j.engfracmech.2026.112173

A local comparison of the virtual crack closure technique and a cohesive zone model in calculating the strain energy release rate for large and curved delaminations

L. M. Martulli[1]*, L. G. Salvi[1], A. Bernasconi [1], Albert Turon[2], Laura Carreras[2]

[1] Politecnico di Milano, Mechanical Engineering Department, Via La Masa 1, 20156 Milano, Italy

[2] AMADE, Polytechnic School, University of Girona, Universitat de Girona 4, E-17003 Girona, Spain

*Corresponding author: lucamichele.martulli@polimi.it

Abstract

The two most common techniques to predict delamination in composites are the Cohesive Zone Model (CZM) and the Virtual Crack Closure Technique (VCCT). These were compared in previous works by only analysing the load-displacement response of different specimens. As shown in this work, this is not sufficient since local computations of the Strain Energy Release Rate (SERR) can be significantly different if large and curved delaminations are involved. This work presents an in-depth comparative strategy based on a local SERR comparison between VCCT and CZM. This strategy was used to compare the two techniques for a non-standard specimen featuring large and curved delamination fronts loaded under mode I and shear modes. A total of 75 SERR distributions show how significant differences may arise between the two techniques. Compared to the current literature, we were able to highlight the importance of considering the SERR instead of global descriptors in comparing the two techniques. This work thus highlights strengths and criticalities of the VCCT and CZM, suggests possible sources of inaccuracies and provides useful guidelines for their better use.

Keywords: Delaminations; Computational fracture mechanics; Cohesive Zone Modelling; Virtual Crack Closure Technique.

1 Introduction

Delamination is the most common and dangerous failure mechanism of composite laminates, especially under fatigue loadings. This failure mode occurs when adjacent plies of the laminate separate from each other: the resulting delamination front may start to propagate without noticeable visual changes in the laminate. Modelling this phenomenon is thus crucial, and design against delamination is still an excellent

preventive mitigation strategy. Currently, the two most common techniques used in Finite Element (FE) analyses for this task are the Cohesive Zone Models (CZM) and the Virtual Crack Closure Technique (VCCT). CZM is based on the use of cohesive elements, whose constitutive law is in the form of a Traction-Separation Law (TSL). TSLs are characterised by a stiffness-reducing damage variable, which allows CZM to model a non-linear fracture process zone. Conversely, VCCT is a linear elastic fracture mechanics approach that computes the Strain Energy Release Rate (SERR) at the delamination front. As a result, a non-linear process zone cannot be reproduced. Moreover, the technique must be coupled with a fracture criterion to reproduce the delamination propagation: the most common approach is to compare the computed SERR with an input fracture toughness to evaluate the possible delamination propagation. More details on both the VCCT and the CZM are widely available in the literature [1–4], but the general features can be summarised in the following:

- Input parameters for VCCT are generally simpler, as it requires only the fracture toughness of the considered interface. CZM require the definition of all the parameters describing the TSL.
- Both techniques require the identification of the fracture plane. However, VCCT also requires the presence of an initial delamination, while CZM does not.
- VCCT is generally observed to be more mesh dependent than CZM.

Another technique often considered when discussing delamination modelling is the extended FE Method (XFEM), a meshless extension of the FE [1,5]. The technique, however, mainly aims at modelling a discontinuity (like a delamination) within elements: it is not a damage or failure criterion, but rather requires their implementation. Therefore, for the purpose of the present work, XFEM is introduced only for the discussion of the available literature.

Several works in the literature compared the performance of CZM and VCCT in predicting delaminations and adhesive debonding, a very similar problem. Heidari-Rarani and Sayedan [6] compared CZM, VCCT and their use via XFEM in 2D and 3D analyses for a Double Cantilever Beam (DCB) specimen, which is loaded in mode I. As shown in Figure 1, all approaches led to reasonable results and agreed with the experimental evidence (provided in [7]). In general, the simulations predicted both the initial linear elastic response and the delamination propagation phase (where the load decreases with increasing

displacement), while discrepancies are present in the transition between the two stages, near the peak load. Moreover, the simulations employing VCCT showed a noisy "sawtooth" response, with the load oscillating significantly more than that predicted by simulations employing CZM. Liu et al. [8] extended the analysis to also cover mode II and mixed-mode loading with very similar results: a good agreement in the initial and propagation response, and a slight discrepancy in the transition phase, with simulations generally being stiffer (higher reaction load to applied displacement). VCCT generally results in higher peak loads and a propagation phase with significant oscillations. Similar comparisons with equivalent results can be found in [9–12].

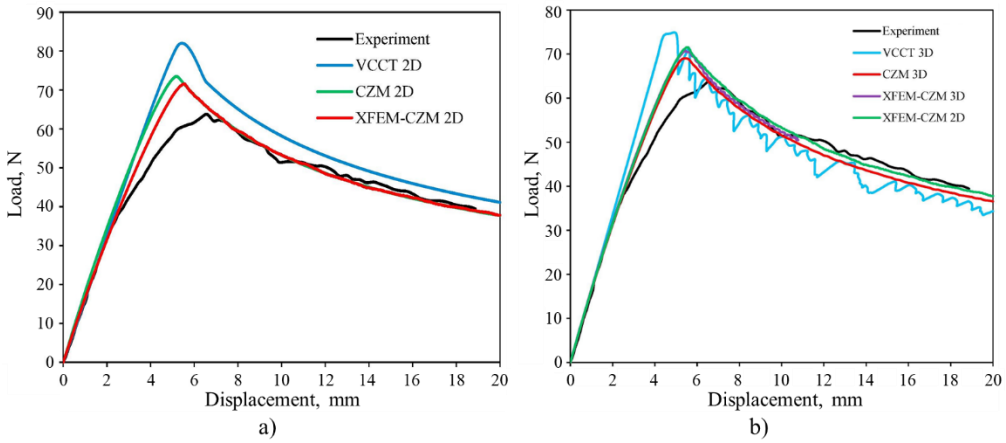

Figure 1: Comparison of VCCT, CZM and their implementation via XFEM for a) a 2D simulation and b) a 3D simulation of a DCB specimen. Reprinted from [6] with permission of Elsevier.

Some works also investigated the fatigue capabilities of both approaches. CZM usually requires the development of a dedicated subroutine [13], while numerical tools are available for the VCCT [14–16]. Pirondi et al., in different related works [17–20] compared both approaches for fatigue predictions of debonding in adhesive joints. The considered specimens were the DCB for mode I, an End-Load Split (ELS) for mode II and a mixed-mode ELS for mixed-mode loadings. The two techniques showed relatively comparable results in terms of globally applied SERR with the number of cycles. Delamination propagation, however, was faster for CZM in the DCB and ELS cases: this appears in contrast with the static results observed earlier, where the VCCT produced higher loads. However, the discrepancy was generally lower than 30%, which for fatigue problems can be considered low.

Other comparisons of both VCCT and CZM for problems other than delaminations in composites are available [21,22]: these works generally confirm the above results with no substantial differences.

As outlined, the literature comparing VCCT and CZM is consistent and quantitatively relevant. However, all these comparisons present two common limitations. First, all these works compare the techniques for simple and standard specimens: while this allows to consider different fracture modes, the analysed delamination fronts and their evolution are often simple and straight. [23][24]In this regard, to the best of our knowledge, only Safaei et al. [25] presented a comparison between VCCT and CZM (both implemented via sequential algorithms) for a large and curved delamination front. Interestingly, the CZM predictions significantly outperformed the VCCT ones; the reason for such discrepancy was attributed to the SERR concentrations caused by the discontinuous description of the delamination front by the VCCT (this issue is elaborated in Section 2.1 of this work). With composite laminates being progressively adopted in large structures, like wind blades [23] or airplane wings [24], the occurrence of macroscopic delaminations with arbitrarily shaped fronts is not negligible [26–28]. These can arise as micro-defects growing due to fatigue loading or due to impact. As we will highlight in this work, these macroscopic fronts are also the ones more difficult to analyse with current numerical techniques. As a result, considering these defects in the design phase may lead to safer and more efficient composite structures, although such approach is challenging. Secondly, all the comparisons consider global descriptors: the load-displacement curve is generally the most used; other options are the global SERR calculated analytically for the whole specimen, the delamination length, or the SERR evolution with the number of cycles, for fatigue problems. These global descriptors are an indirect indicator: a more direct indicator would compare the local severity of the delamination front along the front itself. In particular, comparing the SERR along a delamination front would better explain the analogies and discrepancies between the two techniques, which are so far only observed but not understood. This has implications in the engineering practice as well: fatigue predictions using VCCT and CZM are generally performed by implementing Paris-like laws, in which the SERR is raised to powers larger than 1. As a result, small discrepancies in the SERR can lead to large variations of the predicted life, thus highlighting the importance of an accurate SERR computation. A similar example is related to crack arresting problems, in which a propagating crack can be stopped by a local reduction of the SERR [29,30]: a numerical tool used in this context must ensure a correct SERR computation.

This work thus aims to fill this knowledge gap by comparing the CZM and the VCCT in the local computation of the SERR along the delamination front. A specific methodology was thus developed,

aiming to compare the SERR for all modes of fracture. This methodology, described in Section 2, was designed also to overcome the three main obstacles related to this comparison: the discontinuous description of the delamination front for VCCT, the lack of the SERR as output of cohesive elements and the merging of mode II and mode III properties and loads into a generic shear mode by the CZM. Moreover, a non-standard specimen, described in Section 3, was considered. This was used as opposed to the narrow specimens generally adopted in the literature, which result in straight delamination fronts with a limited curvature. Conversely, the non-standard specimen used in this work can produce highly curved delamination fronts. In this work, we were able to achieve fronts with curvature radii comparable to the semi-width of the specimens. The results of the comparison are presented and discussed in Section 4.

Overall, the present work first compares for the first time the VCCT and CZM local measurements of the SERR for large and curved delamination fronts. This provides additional insights into both formulations and techniques, leading to the identification of best modelling practices and aiding the identification of current drawbacks to be addressed in future developments.

2 Materials and methods

2.1 Adopted case study

The presented strategy was applied to quasi-static case studies. Non-standard specimens were considered for the comparison: a partially Reinforced DCB (R-DCB), mainly loaded in mode I, and a partially Reinforced ELS (R-ELS), mainly loaded in mode II and mode III. Both specimens were previously introduced in other works: the R-DCB was designed, manufactured and tested [31], and thus provides an experimental validation to this work; the R-ELS was designed and used as a numerical exercise in [32], but no experimental evidence is available. Both specimens have very similar geometrical features, but different dimensions: they consist of a large panel which features an initial delamination on one of the shorter edges; smaller reinforcing plates are bonded on each side of the panel to influence the shape of the delamination growth. Both the panel and the reinforcing plates are made of unidirectional carbon fibre laminas oriented parallel to their longer edges (X-direction in Figure 2). The specimens are schematically shown in Figure 2, while the geometrical details are reported in Table 1.

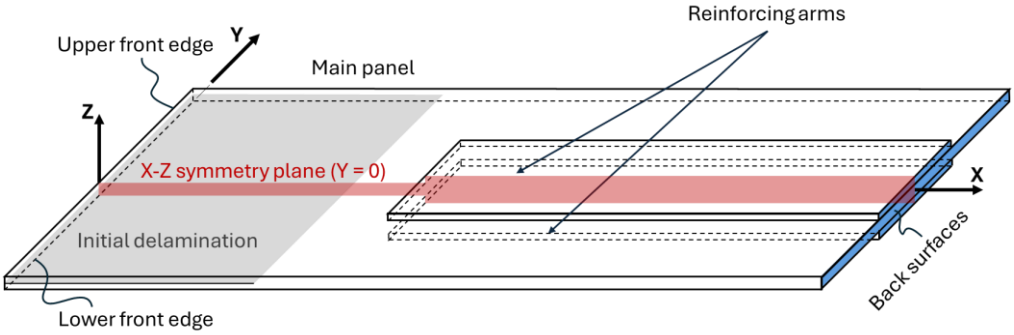

Figure 2: The non-standard specimens adopted in this work[31,32].

Table 1: Geometrical details and boundary conditions for the R-DCB and the R-ELS simulations. The nomenclature refers to Figure 2. U_i and θ_i refer to a displacement and a rotation along/around the i-axis, respectively.

	R-DCB	**R-ELS**
Geometrical details		
Main panel dimensions	175 mm x 60 mm x 3.02 mm	140 mm x 60 mm x 3.02 mm
Reinforcing plates dimensions	120 mm x 25 mm x 1.51 mm	85 mm x 25 mm x 1.51 mm
Initial delamination length	35 mm	40 mm
Boundary conditions		
Upper front edge	$U_x = 0$ mm; $U_z = 15$ mm $\theta_x = \theta_z = 0$	-
Lower front edge	$U_x = U_z = 0$ mm $\theta_x = \theta_z = 0$	$U_z = 30$ mm $\theta_x = \theta_z = 0$
Back surfaces	$U_y = 0$ $\theta_x = \theta_y = \theta_z = 0$	$U_x = U_y = U_z = 0$ mm $\theta_x = \theta_y = \theta_z = 0$

Abaqus 2024 was used in all simulations of the present work [15]. The comparative methodology described below requires running simulations using either VCCT or CZM. Details on the adopted mesh and element types for both types of simulations are reported below, in their relative section (Section 2.3.1 for VCCT and Section 2.3.2 for CZM). In both cases, a mesh-sensitivity analysis was performed to ensure the accuracy of the obtained results. This aimed to match the experimental load-displacement curve for the DCB case: the whole curve was considered for CZM simulations. This was not possible for VCCT simulations, since these were run with a nearly infinite fracture toughness. Therefore, for VCCT simulations, the mesh was refined until no variations of the SERR were observed. For both cases, the

imposed boundary conditions are reported in Table 1. In all simulations, a frictionless contact was used to model the contact between the delaminated areas, while the reinforcing plates were perfectly tied to the main panel. The elastic material properties of the main panel and the reinforcing plates are reported in Table 2. For CZM simulations, bilinear TSLs were considered, whose properties are also reported in Table 2; note that a BK law for the toughness dependence on the mode-mixity is used [33] (η is the fitting exponent). An infinite toughness is considered in the VCCT simulations (as explained in Section 2.3.2).

Table 2: Material properties adopted in the simulations. For the elastic properties: E_i indicate Young's moduli, G_{ij} shear moduli, ν_{ij} Poisson's moduli. For the TSLs: G_{ic} are fracture toughnesses, η is the BK law fitting exponent, τ_i are the maximum tractions and K_i are the penalty stiffnesses.

Elastic properties of the main panels and the reinforcing arms					
E_1 (GPa)	$E_2 = E_3$ (GPa)	$G_{12} = G_{13}$ (GPa)	G_{23} (GPa)	$\nu_{12} = \nu_{13}$ (-)	ν_{23} (-)
120	10.5	5.3	3.5	0.3	0.51
Cohesive properties for the R-DCB simulation					
G_{Ic} (mJ/mm^2)	G_{IIc} (mJ/mm^2)	η	τ_1 (MPa)	τ_2 (MPa)	$K_I = K_{II}$ (N/mm)
0.266	1.002	2.73	30	60	10^6
Reference cohesive properties for the R-ELS simulations					
G_{Ic} (mJ/mm^2)	G_{IIc} (mJ/mm^2)	η	τ_1 (MPa)	τ_2 (MPa)	$K_I = K_{II}$ (N/mm)
2	2	1	70	70	10^5

An additional R-ELS comparative analysis is performed, using half of the cohesive strengths τ_1 and τ_2 respect to those indicated in Table 2 and thus resulting in a doubled cohesive zone: this is the one with all cohesive elements having a $0 < d_e < 1$. As explained in Section 2.3, the lines having equal d_e (iso-damage lines) are used as delamination fronts in the VCCT simulations. Therefore, although unrealistic, this extended cohesive zone causes a larger separation between the analysed delamination fronts and thus leads to a better understanding of the involved numerical calculations.

Overall, three comparative analyses are performed:

1. A comparison on the R-DCB;

2. A comparison on the R-ELS with the parameters reported in Table 2;

3. A comparison on the R-ELS with the parameters reported in Table 2 but with half of the cohesive strengths τ_1 and τ_2. For the rest of the paper, this analysis is referred to as R-ELS2.

2.2 Limitations to overcome

As previously mentioned, a meaningful comparison in the SERR computations between VCCT and CZM is hampered by three main obstacles. A comparative methodology was thus designed to overcome these obstacles, which thus need a dedicated section in the present work.

The first obstacle to a meaningful comparison, is related to the discontinuous node-based description of the delamination front when adopting VCCT: this is even more important for large and curved delamination fronts, i.e. fronts presenting curvature radii comparable to the semi-width of the specimen. In these cases, a "staircase" model of the delamination front is obtained, since the FE mesh is rarely conformal to the delamination front. This is schematically represented in Figure 3, where a generic curved delamination front (Figure 3a) would be described by the VCCT as a discontinuous staircase by a non-conformal mesh (see Figure 3b). This inaccurate description causes numerical SERR concentrations at the "*corner nodes*" of the delamination front, indicated in Figure 3b: in these nodes, an unrealistically higher SERR is computed. This is a known issue in the literature: we believe it is one of the causes for which, for the same simulation, the CZM outperformed the VCCT when implemented in a sequential algorithm for fatigue propagation [16,25]. Nevertheless, its impact will be further elaborated and analysed in this work in Section 2.3.2. Moreover, a discontinuous description of the delamination front causes discontinuities in the definition of the directions parallel and perpendicular to the delamination front, i.e. the directions of the mode II and the mode III loadings, respectively (see Figure 3b). Note that, for corner nodes, these directions are not even definable. Overall, the discontinuous description of the delamination front in VCCT simulations causes higher values of the SERR and prevents its accurate mode II and mode III decomposition. Regarding CZMs, a generally lower mesh sensitivity makes this problem less detrimental. Indeed, the suitability of a non-conformal mesh to the problem adopted in the present study were demonstrated in [32,34,35].

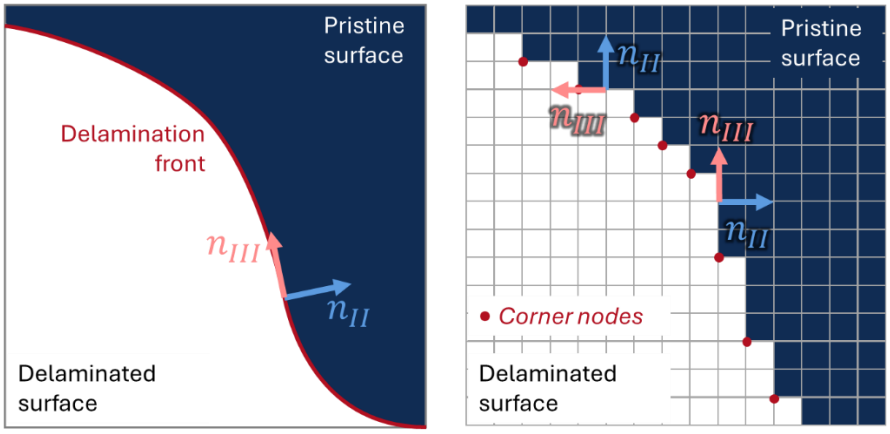

Figure 3: a) a curved delamination front and b) its discontinuous description in a non-conformal FE mesh. In the figure b), the grid represents the FEs and nodes. n_{II} and n_{III} are the unit-vector for the mode II and mode III directions, respectively.

The second and third obstacles to a VCCT/CZM meaningful comparison in SERR computation are related to the CZM: these are the lack of distinction between the shear modes and the extraction of the SERR itself. The former is easy to describe: most CZM formulations combine mode II and mode III displacements and tractions, and thus the relative TSLs, into a unique one. As a result, no distinction between the two is made [2,36,37].

Regarding the last obstacle, TSLs generally implement a maximum traction criterion, with displacement at damage onset and failure calculated via the fracture toughness: the SERR is thus neither needed nor calculated. The need to implement fatigue propagation laws into CZMs, however, drove the scientific research into overcoming this issue. Considering a bilinear TSL and a generic point (δ^*, τ^*), Figure 4a and Figure 4b show two important quantities: the specific dissipated energy ω_d and the total specific work ω_{tot} [32]. To adopt Paris-like fatigue laws, the SERR was sometimes assumed to be equal to ω_{tot} [25,36,38]. While this often led to accurate fatigue predictions, the two quantities are conceptually different. The total specific work ω_{tot} represents the work performed by the external forces on a specific location of the interface until a certain moment in time: it is a local quantity and depends on the load history on that point. Conversely, the SERR is the energy released by the whole system (structure plus loads) upon an infinitesimal advancement of the delamination front, i.e. the derivative of the energy stored in the system over the advancement [39]: it is thus an instantaneous and global quantity. For this reason, the ω_{tot} can be computed for each integration point of the cohesive zone regardless of the neighbouring elements; conversely, extracting the SERR requires information from all the elements of the

cohesive zone [38,40,41]. While computing ω_{tot} is thus easier, Bak et al. [41] noted how adopting it instead of the SERR in a Paris-like law would result in a different delamination propagation for each integration point, which is not physically coherent. Ultimately, the two quantities were shown to be different in the initial nucleation phase (where several cohesive elements are loaded in the elastic region) [38] and for coarser meshes [38,40,41].

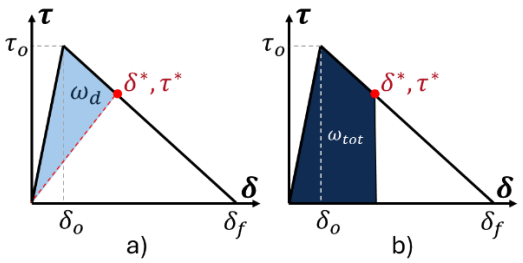

Figure 4: Energetic parameters in TSLs: a) the dissipated energy ω_d and b) the total specific work ω_{tot}.

2.3 Overall methodology

The comparative methodology adopted in this work is schematically described in Figure 5. First, the reference CZM simulation is performed using the model described in [34] and implemented via an Abaqus user subroutine UEL [15]: further details on this simulation and the implemented model are reported in Section 2.3.1. The complete load-displacement curve of the analysed structure is thus extracted. Since the comparison can only be performed locally on specific points of the curve, that is on specific increments of the CZM simulation, points of interest along the obtained load-displacement curve are selected for the comparison.

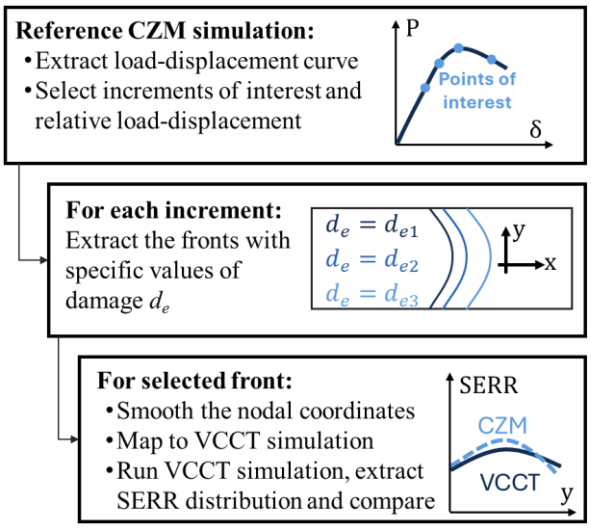

Figure 5: Schematic representation of the comparative methodology adopted.

Each of these increment presents a unique configuration of the cohesive zone and, thus, a damage distribution from which iso-damage lines can be extracted. Each of these lines can be used to define a delamination front in an independent VCCT simulation. A virtually infinite toughness is imposed to prevent the delamination propagation allowing for the calculation of the local SERR values. Imposing an infinite toughness is indeed required for an accurate SERR estimation but may cause unreasonably high SERR. This is an acceptable risk given the scope of the present work, which is not to predict delamination propagation, but rather compare the SERR computations.

Given the different meshes used in the CZM and the VCCT simulations, a direct mapping of the iso-damage lines as delamination front for a VCCT simulation would result in a discontinuous front description and consequently into the creation of corner nodes (see Section 2.2). Therefore, an intermediate smoothing step is performed, as described in Section 2.3.2.

Once the VCCT simulation of a specific delamination front is obtained, SERR values can be calculated and compared with the corresponding values obtained from the reference CZM increment. Repeating the procedure for all the selected iso-damage lines (i.e. delamination fronts in the VCCT simulations) allows to compare the CZM and VCCT SERR calculations for a specific point of the load-displacement curve. This can thus be further repeated for all the points of interest of the curve.

As mentioned earlier, three simulations are performed: a R-DCB, a R-ELS with standard cohesive parameters and a R-ELS with halved cohesive strength. For all simulations, five increments or points of the load-displacement curves were considered interesting for the scope of the present analysis. These were selected to consider different moments of the delamination propagation, thus spanning the non-linear portion of the load-displacement curve. In all cases, five damage values of interest were selected for the iso-damage lines extractions: 0, 0.25, 0.5, 0.75, 1. Note that 0 and 1 correspond to the boundaries of the cohesive zone, while the others were selected as intermediate and equally spaced values to uniformly cover the full range.

Overall, the whole procedure compared the VCCT and CZM readings for 75 delamination fronts.

2.3.1 Cohesive zone model implementation and simulations

This work adopts the CZM implementation proposed by Carreras et al. [32,34]. This section will describe the features of the model that allows it to overcome the CZM limitations identified in Section 2.2; for the full details, the readers are referred to the original article.

An energy-based expression of damage is first adopted, that is:

$$d_e = \frac{\omega_d}{G_c} \qquad \text{Eq. 1}$$

where ω_d is the dissipated specific energy (introduced in Figure 4a). This damage definition features a linear trend from 0, when the displacement jump δ is equal to δ_0, and 1, when the displacement jump is equal to its failure value δ_f. Each element of the cohesive zone will thus be characterised by a specific value of d_e.

In linear elastic fracture mechanics, any front is assumed to grow along a direction perpendicular to itself. In the case of CZM, this is not directly applicable, since the sharp delamination front is replaced by the non-linear cohesive zone. Therefore, the growth direction θ_1 is identified as the direction perpendicular to the iso-damage lines, which is the lines having equal values of d_e in the cohesive zone. Considering Figure 6 [34], this is expressed as:

$$\theta_1 = -\nabla D_e \qquad \text{Eq. 2}$$

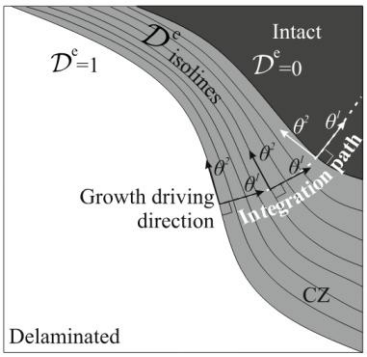

Figure 6: The front growth direction as the direction perpendicular to the iso-damage lines. Reprinted from [34] with permission of Elsevier.

With the identification of a growth direction for the delamination front, the two CZM limitations previously identified can be solved (see Figure 6) [34]:

- The growth direction θ_1 is associated with the fracture mode II; consequently, the direction θ_2 perpendicular to it and tangent to the iso-damage lines is associated to the fracture mode III. This allows to clearly distinguish between the two shear modes. The mode I is unaltered, being defined by the direction perpendicular to the delamination plane.
- The SERR is computed using the J-integral, which is a popular technique for this task [42]. The J-integral directly equates the SERR and has been successfully implemented in CZMs that do not assume the SERR to be equal to the total specific work ω_{tot} [17,41,43]. For the J-integral calculation, the stresses and displacements are locally available through each cohesive element, while all the θ_1 directions are considered as integration paths. This is equivalent to consider the cohesive zone as composed of infinite slices of infinitesimal thickness in which the delamination propagates along θ_1. Mathematically, this translates into the Eq. 3 for the calculations of the J-integral components, where g11 is the first component of the covariant metric tensor, σ_{ij} are components of the stress tensor and δ_i are the displacement jump components; δ_i is defined in Eq. 4, with u_i^+ and u_i^- being the displacements of the upper and lower delaminating surfaces, respectively.

$$J_I = -\frac{1}{\sqrt{g_{11}}}\int_{CZ}\left(\sigma_{33}\frac{\partial\delta_3}{\partial\theta_1}\right)d\theta_1$$
$$J_{II} = -\frac{1}{\sqrt{g_{11}}}\int_{CZ}\left(\sigma_{13}\frac{\partial\delta_1}{\partial\theta_1}\right)d\theta_1 \qquad \text{Eq. 3}$$
$$J_{III} = -\frac{1}{\sqrt{g_{11}}}\int_{CZ}\left(\sigma_{23}\frac{\partial\delta_2}{\partial\theta_1}\right)d\theta_1$$

$$\delta_i = (u_i^+ - u_i^-) \qquad \text{Eq. 4}$$

All CZM simulations performed in this work adopts a mesh with a maximum element length of 0.75 mm. In all simulations, a minimum of 4 elements in the cohesive zone was ensured, following the guidelines in the literature [40,44].

2.3.2 Front mapping and VCCT simulations

In the cohesive zone, specific iso-damage lines are most often found in-between mesh nodes without passing through any one of them. Thus, the iso-damage lines are remapped using the coordinates of the nodes whose damage is within a tolerance to the selected value. Additionally, since the CZM does not

require a conformal mesh to produce a smooth front (and more in general smooth iso-damage lines), the CZM simulations are implemented on simple orthogonal-grid meshes. Therefore, directly mapping the CZM iso-damage lines as VCCT delamination front would result in the presence of corner nodes and the limitations described in Section 2.2 due to a staircase-like description of the front. To create a smooth and continuous delamination front for the VCCT simulations, the iso-damage lines are smoothed. A first comparison between a spline interpolation, a polynomial interpolation and a moving average is performed. As shown in Figure 7a, the moving average algorithm with a window size of 15 outperformed the other algorithms and was thus selected for the rest of the work. In this work, a window size of 15 was found as the most suited; nevertheless, a more comprehensive description of the smoothing method, with a dedicated sensitivity analysis to the smoothing window size, is presented in [45]. The resulting smoothed curve, composed of several points, is merged in a single continuous curve (this can be easily done in Abaqus as in any other advanced CAD or FE software). This prevents the introduction of the geometrical points into the model and their subsequent transformation into nodes, which would alter the final mesh. In this work, the delamination front is mapped as a "partition" in Abaqus CAE [15]. To highlight the importance of this smoothing step, two R-ELS VCCT simulations were performed with the smoothed and the non-smoothed delamination front of Figure 7a. The resulting SERR calculations are compared in Figure 7b. As shown, the non-smoothed delamination front results in an unrealistically discontinuous SERR distribution, quite uncorrelated with the one obtained after smoothing. Thus, any comparison of a continuous distribution (like that coming from an equivalent CZM simulation) with the non-smoothed results would be meaningless. Moreover, note that for both mode I and mode II, the peaks caused by the SERR concentrations are often significantly higher than the smoothed distribution. For VCCT simulation with finite fracture toughness or fatigue simulations, this would result in a premature propagation of the delamination front: this confirms that the presence of the SERR concentrations contributed to the early front propagation recorded in [16] and generally lowers the accuracy of VCCT predictions.

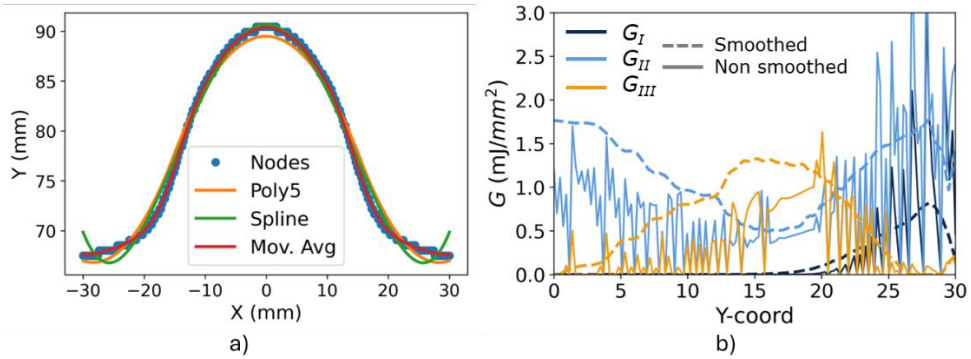

Figure 7: a) Tested smoothing algorithms on a delamination front described by nodal coordinates: "Poly5" stands for a 5th degree polynomial smoothing, "Mov. Avg" stands for moving average. b) a comparison in the computation of the SERR for a delamination front before and after smoothing.

Given the mesh-dependent nature of VCCT, additional care must be taken into creating a conformal mesh. Given that the mesh is created after the mapping of the delamination front, a conformal mesh is automatically ensured. A 0.5 mm seed is first considered along the delamination front. Moreover, two rows of 0.5 mm x 0.5 mm elements are imposed on both sides of the delamination front (four rows in total). In this way, a region of very fine mesh, with 0.5 mm average element size, is ensured in the region surrounding the whole delamination front. Additional simpler partitions are imposed to ensure a structured mesh everywhere else in the part. Finally, 4 elements through the thickness direction were considered for all VCCT simulations. The elements used are continuum shell C3D8R [15]. As an example, Figure 8 shows the mesh of an R-ELS2 VCCT simulation (28.0933 mm displacement, 0.5 damage). Given the importance of the mesh in the VCCT simulations within the present work, all the VCCT meshes are freely available for download as Abaqus .inp file in [46].

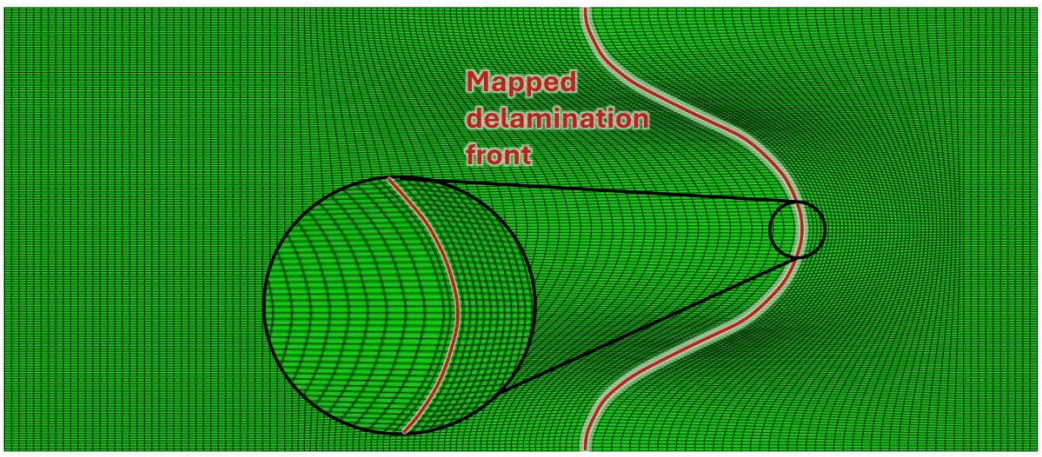

Figure 8: An example of a mesh conformal to the delamination front used in a VCCT simulation.

2.3.3 Summary of the calculation of the SERR by the selected methods

To assist the readability of this work, we have summarised briefly in this section the main differences between the VCCT and selected CZM approach in calculating the SERR.

In VCCT, the SERR is evaluated within a linear elastic fracture mechanics framework by assuming a sharp delamination front that advances by a small, discrete increment. The front is assumed to propagate self-similarly. The local SERR is obtained from the work required to close the delamination over this increment, using nodal forces at the front and relative displacements behind it. VCCT is thus very sensitive to the discrete nodal description of the front. In three-dimensional problems, the decomposition into mode I/II/III further relies on the definition of a local crack-front coordinate system (normal and tangential directions to the front). In the context of curved delamination fronts, this coordinate system can become ill-defined or discontinuous due to its staircase-like representation (typical of non-conformal meshes and strongly curved fronts, see Figure 3b). Under these conditions, corner nodes and abrupt changes in local orientation can produce artificial SERR peaks and unstable mode partitions.

In CZM a finite fracture process zone is considered ahead of the front; this zone is modelled via a traction-separation law. The SERR is not directly computed by standard cohesive formulations. In the present work, the local SERR is obtained through a mode-decomposed J-integral formulation evaluated across the cohesive zone, where the crack-growth direction is defined from the damage-field gradient (normal to iso-damage lines, see Figure 6).

3 Results and discussion

In this section, a critical discussion of the results is presented by showing some representative comparisons. Nevertheless, all 75 comparisons, together with the reference load-displacement curves, were collected in a supplementary file attached to the present paper. The supplementary results file and the present discussion and images all show half of the analysed R-DCB and R-ELS, exploiting their symmetry. The numerical data of the results are also available at [46]. Note that, for all simulations, the load-displacement combinations predicted by the different VCCT simulations are in line with the CZM one.

3.1 R-DCB

Figure 9 compares the numerical CZM simulation of the R-DCB with the experimental data of [31]. As shown, the numerical simulation can follow accurately the experimental results, proving its capability of reproducing the performed tests. The simulation struggled to complete and reach 15 mm of applied displacement; however, applying the comparative methodology up to the achieved 8 mm is still possible and informative. Moreover, the load-displacement combinations predicted by the different VCCT simulations are also in line with the CZM curve, as reported in the supplementary results file.

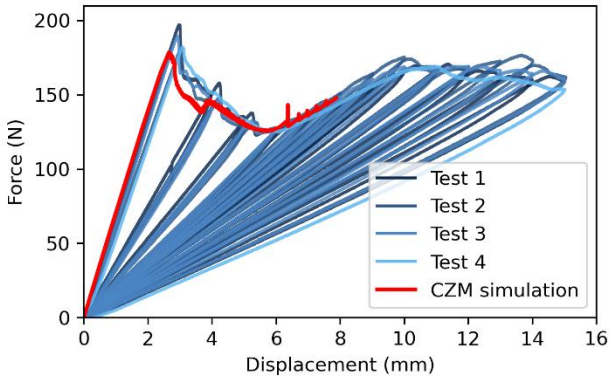

Figure 9: Experimental and numerical load-displacement curves of the R-DCB.

The results showed in the supplementary results file first highlight a small cohesive length, which is coherent with both the data used and a general smaller process zone for mode I than the shear modes [44,47,48]. The compact size of the cohesive zone produces small variations in the remapped delamination fronts and thus small variations in the load-displacement combinations obtained from the VCCT simulations. Said sequence of load-displacement points obtained at different iso-damage value lie on top of the CZM load-displacement curve, showing a good general agreement between the two approaches.

As expected, in the R-DCB simulations only the mode I SERR G_I has significant non-zero values. These show only minor variations between the analysed damage fronts and generally oscillate around 0.3 mJ/mm^2. For the first three displacements considered, CZM and VCCT readings tend to agree on similar values and trends, although the VCCT showed more oscillations, especially close to the edge where the fronts start to curve (see Figure 10a, as an example). For the latter two displacements, the fronts were significantly more curved: as a result, the VCCT readings show significantly higher and more frequent spikes (see Figure 10b, as an example). This is likely an indication that a more targeted and dedicated

smoothing strategy is required. A similar conclusion is present in [45], which highlights how a universal smoothing strategy for any front is still not identified. Nevertheless, G_I values from the VCCT can still be analysed, especially considering the improvement from the unsmoothed case of Figure 7b. For this reason, we preferred not to pursue an individual smoothing strategy for each front.

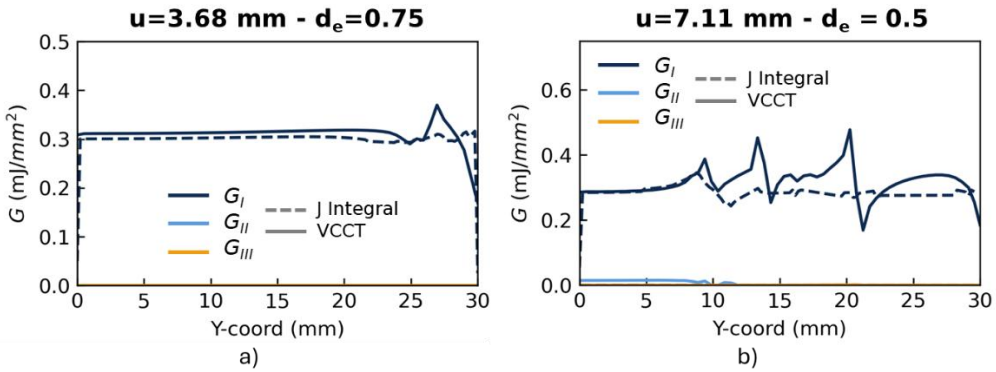

Figure 10: SERR readings of the R-DCB from the CZM and the VCCT simulation for an applied displacement and d_e of, respecttively, a) 3.68 mm and 0.75 and b) 7.11 mm and 0.5.

Overall, the computations from the VCCT and the CZM tend to be in general agreement when the front is smoothed properly. The maximum discrepancies between the two computations occurs in correspondence of the concentrations of the SERR. It is thus likely that the quality of the front is the main cause for discrepancy between the SERR computed by the two techniques. As a result, discrepancies are more common when the front is more curved.

Finally, note that the small size of the cohesive lengths caused higher gradients of d_e. Since the plots were obtained by searching for values of d_e within a 0.05 mJ/mm^2 range, some CZM fronts appear incomplete, as not many nodes fell into the searched range. This is more common in the limit fronts, i.e. those for which d_e=0 or d_e=1.

3.2 R-ELS with standard and doubled cohesive lengths

Unlike for the R-DCB case, no experimental data is available for the R-ELS. While this is a limitation of the present work, a meaningful comparison of the two numerical approaches is still possible.

Both the R-ELS and the R-ELS2 simulations are characterised by a larger cohesive length, as expected for delaminations under mode II loading [44,47,48]. This was intentional, especially for the R-ELS2, as the analysis of these two cases proved more informative, with respect to the R-DCB, allowing for a grater separation between the iso-damage lines in the cohesive zone.

All simulations are characterised by a significant presence of both mode II and mode III SERR components, while mode I is generally smaller and even negligible in the central 30 mm of the specimens. Interestingly, when the VCCT and the CZM compute different SERR components, these are not necessarily complementary: lower values of the mode II SERR are not associated to higher values of the mode III, and vice-versa. This implies that, when the two techniques do not match, they compute different values of the total applied SERR (i.e. the sum of the three components) and the discrepancy between the two methods is not caused by a decomposition mismatch between the shear modes.

For all simulations, the presence of the reinforcement seems to have a strong impact on the SERR components. In particular, two regions can be identified mostly surrounding its edges, highlighted as A and B in Figure 11.

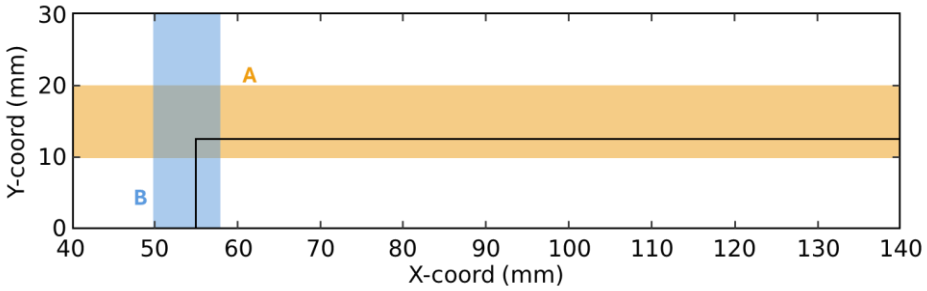

Figure 11: Regions of influence of the reinforcement.

In region A, defined by 10 mm < Y < 20 mm, the reinforcement seems to cause a trough in the mode II and a peak in the mode III components. These are shown for the example of the R-ELS2 simulations in Figure 12. Both the mode II trough and the mode III peak are present even ahead of the reinforcement (X < 55 mm), thus likely influencing the delamination evolution before the front reaches it. This causes the fronts to start changing curvature before reaching the reinforcement, which was also experimentally observed for the mode I R-DCB case [31]. The peaks and troughs are also often the location where the maximum discrepancies between the techniques are found, if present. This is visible in Figure 12a-d, especially for the mode III peak. Figure 12a also shows an example of the aforementioned non-complementarity of the mode II and mode III SERR components: at Y=15 mm, the VCCT and the CZM simulations computed similar G_{II} but different G_{III} values, thus computing a different total SERR.

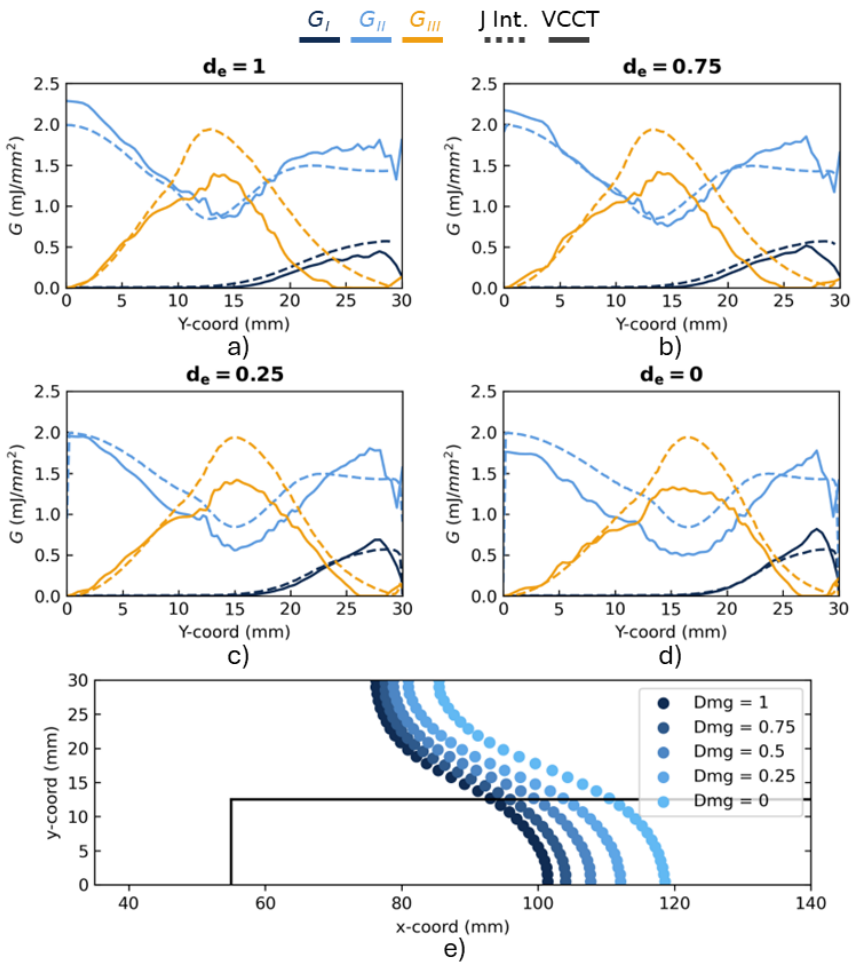

Figure 12: R-ELS2 simulations for an applied displacement of 28.1 mm: a-d) SERR readings and e) delamination fronts.

Region B, defined by 50 mm < X < 60 mm, also appears to be highly affected by the reinforcement. In particular, this region presents the highest discrepancies observed in the SERR computations of the CZM and the VCCT: as shown in Figure 13a, discrepancies as high as 150% can be observed, with the VCCT often computing very high values of G_{II}. Moreover, Figure 13e also shows that the highest discrepancies between the techniques is observed for the $d_e = 1$ and the $d_e = 0.75$ fronts, which present a limited curvature compared to other fronts. For example, the very curved fronts shown in Figure 13e resulted in a significantly smaller discrepancies between the two techniques.

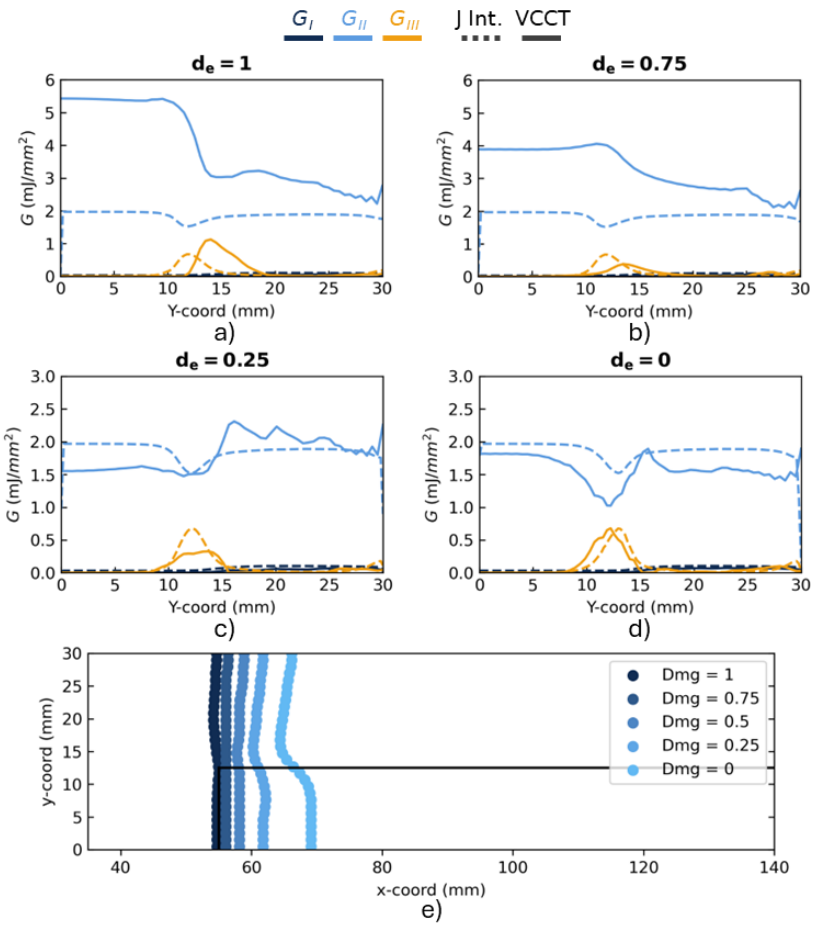

Figure 13: R-ELS2 simulations for an applied displacement of 24.99 mm: a-d) SERR readings and e) delamination fronts.

Such high discrepancies in region B are likely due to the violation of the underlying VCCT assumption of a self-similar delamination growth. Indeed, the VCCT is based on this assumption according to which the shape of the delamination front is not changed when this propagates by one row of nodes. When the fronts are far from region B, both before and beyond it, their propagation conditions are similar to that schematically shown in Figure 14a: in this condition, the self-similarity of the delamination growth is likely respected. Conversely, delamination fronts in region B face a sharp laminate thickness change, as schematically illustrated in Figure 14b. This change of thickness affects the local bending rigidity of the

laminates, and thus the self-similarity of the delamination advancement is likely lost.

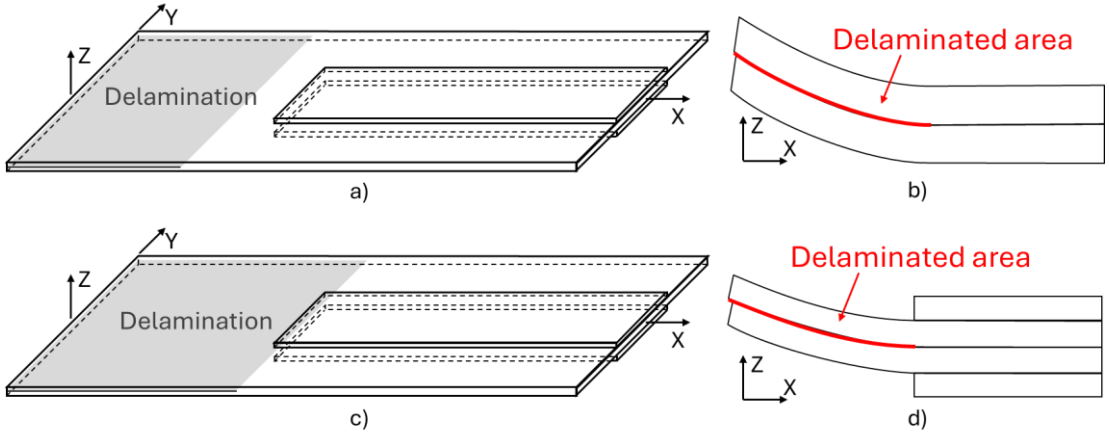

Figure 14: Delaminating fronts that a) respect the self-similar delamination growth and b) schematic representation, or that c) do not respect the self-similar delamination growth and d) schematic representation.

Note that, in region B, significantly higher discrepancies are observed for G_{II} than for G_{III} (see Figure 13). It can be assumed that this is caused by perpendicular orientation of the mode II direction to the edge of the reinforcement in region B: the thickness variation in this direction is more abrupt, thus possibly causing larger deviation from a self-similar growth condition. This hypothesis would also justifies the discrepancies observed in region A, where both G_{II} and G_{III} present some level of discrepancies (see Figure 12): here, the oblique orientation between the delamination fronts and the reinforcement edge the violation of the self-similar growth in both direction II and III. Finally, this hypothesis could also explain the fact that the observed discrepancies are not related to the SERR decomposition, since the total SERR is not preserved: it would rather suggest that the violation of the self-similar delamination growth affects the different modes independently. However, dedicated simulations would be required to further confirm this proposed explanation.

3.3 General discussion

The main difference between the compared VCCT and CZM approaches is the presence of a non-linear process zone, which is completely absent for the VCCT and modelled via the cohesive zone in CZM. Moreover, the adopted reinforced specimens have highlighted another limitation of the VCCT, namely its assumption of a self-similar delamination growth, absent in CZM.

Both these differences seem to have a reduced effect for the R-DCB case, for which a general agreement between the techniques was found. This was likely due to the smaller process zone, common in mode I

conditions. The techniques showed more significant differences in the SERR computation in the case of more curved fronts. However, the discrepancies were mostly due to spikes and irregularities in the VCCT computations (see for example Figure 10b). Therefore, we suggest that this is mostly due to the mesh-dependency of the VCCT, which thus required a finer smoothing strategy for curved fronts.

Interestingly, the two differences between VCCT and CZM mentioned above also had a minor impact on the R-ELS and the R-ELS2 tested, even if much larger process zones were involved. In these cases, minor discrepancies were always observed, which is reasonable given the two different approaches. However, the major discrepancies occurred close to the reinforcement's edges, which suggested that the non-self-similar growth is the main source of these discrepancies. Interestingly, this issue thus seems to be significantly more important than the differences between the techniques and also than the curvature of the fronts. Indeed, straight fronts close to the reinforcement's edge showed higher discrepancies in the SERR readings than highly curved fronts in different areas. This likely appear to be a severe limitation of the VCCT, which should thus be adopted with care in case of complex geometries or evolving fronts.

Finally, all the load-displacements curves presented in the supplementary results file showed a reasonable agreement between the techniques. For the R-ELS and the R-ELS2, the VCCT simulations with higher d_e delamination fronts correctly resulted in higher loads than those of lower d_e. The CZM curve was in all cases encompassed by the VCCT load-displacement combinations. Therefore, the scatter between the five VCCT simulations was proportional to the process zone and was thus minimal for the R-DCB and large for the R-ELS2. The maximum observed discrepancy between the VCCT and the CZM reaction load was about 12%. This discrepancy is in contrast with significantly larger differences in the SERR computations by the two techniques. This highlights the limitation of the common practice of comparing only the global load-displacement curves of two simulations employing VCCT and CZM.

3.4 Implications and limitations of the present work

VCCT and CZM are currently the most adopted techniques to analyse delaminations in composite laminates. The present work has thus several implications in the engineering practice.

First of all, we have demonstrated the importance of not relying exclusively on global descriptors, namely the load-displacement curve, when numerically analysing delaminations: CZM and VCCT can lead to similar estimates of these global descriptors, while computing different local distributions of the SERR.

This has strong implications in design against fatigue: in this case, the SERR readings from either CZM or VCCT are often used in Paris-like propagation laws, which raises the SERR to a power greater than 1 [1,16,17,25,36,41,43]. Any error in the SERR computation is thus amplified, and the accuracy of the readings of the SERR are thus of paramount importance.

Some guidelines in the use of VCCT can also be extracted from this work. First, the importance of a mesh conformal to the delamination front is here stressed; to this end, a general approach based on the front smoothing is here successfully adopted (this is further elaborated in [45]). Moreover, we have also demonstrated the importance of ensuring that the self-similarity of the crack growth is respected when adopting VCCT.

The present work has further implications in the design of composite structures. For example, within a no-growth damage tolerance philosophy, the structure containing defined flaws must be shown to withstand representative repeated loading without detrimental flaw growth for the life of the structure [49,50]. For delamination-type flaws, the SERR along the delamination front can be computed and compared with experimentally measured interlaminar fracture toughness (or fatigue thresholds) to assess delamination onset and growth, and to support no-growth arguments. In this sense, the present work can support the selection of the best numerical method for the task and suggest a better use of it.

Nevertheless, the present work still requires a certain advancement before making a direct impact into industrial practice: additional experimental work would be required to further assist the presented analysis. We have shown the experimental results for the R-DCB, which supports the validity of the VCCT and CZM simulations. Additional experimental data relative to the R-ELS would strengthen our analysis. Nevertheless, note that the focus of the present work is the computation of the SERR, which is not possible to measure directly experimentally nor to compute analytically for this complex specimen. Therefore, we also believe that additional experimental validation of the R-ELS would have led to limited additional insights.

4 Conclusions and future works

This work presents a strategy to compare numerical approaches when modelling delamination in composites, underlining the discrepancies of the computed SERR values. The strategy is applied to a CZM implementing a J-integral formulation and a commercial VCCT approach. The simulations were

performed on a non-standard reinforced specimen, chosen to promote large and curved delamination fronts and including a prevailing mode I and a prevailing shear mode load case.

We first highlighted the main obstacles to such a comparison, namely the discontinuous node-based description of delamination fronts when using the VCCT and the lack of a properly defined SERR and its shear components in the case of CZM. The former issue required a specific front smoothing strategy, while the latter two were overcame by using a previously published J-integral computation. These two improvements were implemented in a comparative approach to compare the SERR computations along iso-d_e lines in the process zone of the CZM simulations. We showed how front smoothing is essential to obtain meaningful SERR computations by the VCCT.

A total of 75 comparative graphs were presented in this work. The main findings of this comparison were:

- For small process zones under prevailing mode I loading, the two technique generally showed similar SERR readings, with the main source of discrepancies being attributed to the VCCT mesh dependency.
- For the specimens loaded mostly under shear modes, the two techniques still showed similar SERR readings, even for large delamination fronts, except in the areas close to geometrical discontinuities. Here, the VCCT showed higher unphysical SERR readings, which we attributed to the violation of the self-similarity of the delamination growth, a major assumption of VCCT.
- The different readings of the SERR components did not compensate each other to obtain a similar total SERR: the differences in SERR components thus implied differences in the total SERR computed by the techniques.
- When using VCCT in delamination analysis it is essential to ensure: 1) the orthogonality of the mesh to the delamination front and 2) the respect of the self-similarity of the delamination growth. In the present work, the latter was caused by strong and abrupt thickness variations.

Even when SERR readings were very different, the compared simulations showed similar load-displacement combinations. This is a critical issue, since the two techniques have been compared so far only on the basis of the global load-displacement curves, which this work shows to be insufficient.

Overall, this work presented an effective comparative strategy between the CZM and VCCT, but also led to a critical analysis of the two techniques showcasing both strength and limitations. However, experimental validation was provided only for the mode-I dominated R-DCB case; while this did not prevent a meaningful comparison between the numerical techniques, experimental data would further support our findings. However, the higher complexity of the mode-II R-ELS test makes this validation more challenging and is left as a future work. Additionally, more industry-relevant cases can also be designed to further compare CZM and VCCT and their SERR evaluations. For example, adopting the comparative technique for an experimentally validated industrial demonstrator can lead to: 1) a deeper assessment of the two techniques for a wider range of loading conditions and 2) a further evaluation of the suitability of the techniques for their use in the industrial practice.

Another future development stemming from this work is the consideration of different formulations of CZMs. The developed comparative strategy can indeed be used to further assess different techniques for the SERR computation: these include, for example, advanced CZM formulations [51,52].

5 References

[1] Pascoe JA, Alderliesten RC, Benedictus R. Methods for the prediction of fatigue delamination growth in composites and adhesive bonds - A critical review. Eng Fract Mech 2013;112–113:72–96.

[2] Turon A, Camanho PP, Costa J, Dávila CG. A damage model for the simulation of delamination in advanced composites under variable-mode loading. Mechanics of Materials 2006;38:1072–89.

[3] Krueger R. Virtual crack closure technique: History, approach, and applications. Appl Mech Rev 2004;57:109–43.

[4] Krueger R. The virtual crack closure technique for modeling interlaminar failure and delamination in advanced composite materials. Numerical Modelling of Failure in Advanced Composite Materials, Elsevier Inc.; 2015, p. 3–53.

[5] Huynh DBP, Belytschko T. The extended finite element method for fracture in composite materials. Int J Numer Methods Eng 2009;77:214–39.

[6] Heidari-Rarani M, Sayedain M. Finite element modeling strategies for 2D and 3D delamination propagation in composite DCB specimens using VCCT, CZM and XFEM approaches. Theoretical and Applied Fracture Mechanics 2019;103:102246.

[7] Heidari-Rarani M, Shokrieh MM, Camanho PP. Finite element modeling of mode I delamination growth in laminated DCB specimens with R-curve effects. Compos B Eng 2013;45:897–903.

[8] Liu R, Yu Z, Nasonov F. Evaluations on VCCT and CZM methods of delamination propagation simulation for composite specimens. Aerospace Systems 2023;6:621–32.

[9] Sindhu BR, Raju J, Kamath K. A comparative numerical study of standard 3D composite plate using virtual crack closure technique and cohesive zone modelling method. IOP Conf Ser Mater Sci Eng 2019;561:012048.

[10] Mollón V, Bonhomme J, Elmarakbi AM, Argüelles A, Viña J. Finite element modelling of mode I delamination specimens by means of implicit and explicit solvers. Polym Test 2012;31:404–10.

[11] Roberts EM, Justusson B, Schaefer J, Wanthal SP. Improved Benchmarking of Cohesive Elements in Abaqus Standard for Predicting Disbond and Delamination in Composite Structures. AIAA Scitech 2021 Forum, Reston, Virginia: American Institute of Aeronautics and Astronautics; 2021.

[12] Gliszczynski A, Wiącek N. Experimental and numerical benchmark study of mode II interlaminar fracture toughness of unidirectional GFRP laminates under shear loading using the end-notched flexure (ENF) test. Compos Struct 2021;258:113190.

[13] Carreras L, Bak BLV, Jensen SM, Lequesne C, Xiong H, Lindgaard E. Benchmark test for mode I fatigue-driven delamination in GFRP composite laminates: Experimental results and simulation with the inter-laminar damage model implemented in SAMCEF. Compos B Eng 2023;253.

[14] Barbero EJ. Introduction to Composite Materials Design. II Edition. Boca Raton (FL, US): CRC Press; 2011.

[15] Dassault Systemès. Abaqus 2024 manual. n.d.

[16] Martulli LM, Bernasconi A. An efficient and versatile use of the VCCT for composites delamination growth under fatigue loadings in 3D numerical analysis: the Sequential Static Fatigue algorithm. Int J Fatigue 2023;170:107493.

[17] Moroni F, Pirondi A. A procedure for the simulation of fatigue crack growth in adhesively bonded joints based on the cohesive zone model and different mixed-mode propagation criteria. Eng Fract Mech 2011;78:1808–16.

[18] Pirondi A, Moroni F. Simulation of mixed-mode I/II fatigue crack propagation in adhesive joints with a modified cohesive zone model. J Adhes Sci Technol 2011;25:2483–99.

[19] Pirondi A, Giuliese G, Moroni F, Bernasconi A, Jamil A. Comparative study of cohesive zone and virtual crack closure techniques for three-dimensional fatigue debonding. Journal of Adhesion 2014;90:457–81.

[20] Giuliese G, Pirondi A, Moroni F, Bernasconi A, Jamil A, Nikbakh A. Fatigue delamination: a comparison between Virtual Crack Closure and Cohesive Zone siulation techniques. The 19th International Conference on Composite Materials (ECCM19), Montréal, Canada, Canada: 2013.

[21] Yu Z, Zhang J, Shen J, Chen H. Simulation of crack propagation behavior of nuclear graphite by using XFEM, VCCT and CZM methods. Nuclear Materials and Energy 2021;29:101063.

[22] Kumar V, Singh A, Kumar Gupta R. Assessing fracture behavior in Composite-Metal bonded joints under opening and sliding Modes: Insights from Experiments, CZM, and FEA. Theoretical and Applied Fracture Mechanics 2024;134:104713.

[23] Martulli LM, Diani M, Sabetta G, Bontumasi S, Colledani M, Bernasconi A. Critical review of current wind turbine blades' design and materials and their influence on the end-of-life management of wind turbines. Eng Struct 2025;327:119625.

[24] Dillinger JKS, Klimmek T, Abdalla MM, Gürdal Z. Stiffness Optimization of Composite Wings with Aeroelastic Constraints. J Aircr 2013;50:1159–68.

[25] Safaei S, Bernasconi A, Carboni M, Martulli LM. A novel implementation of the cohesive zone model for the fatigue propagation of delamination in composites using a sequential static fatigue algorithm. Int J Fatigue 2025;192:108712.

[26] Leciñana I, Carreras L, Renart J, Zurbitu J, Tijs BHAH, Turon A. A simulation strategy for fatigue modeling of delamination in composite structures under multiple loading conditions considering loading history and R-curve effects. Compos Part A Appl Sci Manuf 2024;186:108402.

[27] Daniel PM, Främby J, Fagerström M, Maimí P. A method for modelling arbitrarily shaped delamination fronts with large and distorted elements. Eng Fract Mech 2024;306:110193.

[28] Daniel PM. A strategy for efficient modelling of composite delamination in large structures. Doctoral thesis. Universitat de Girona, 2025.

[29] Amini MR, Shahani AR. Finite element simulation of dynamic crack propagation process using an arbitrary Lagrangian Eulerian formulation. Fatigue Fract Eng Mater Struct 2013;36:533–47.

[30] van de Kerk JJ, de Melo RFV, Bastiani G, Donadon MV, Arbelo MA. A numerical and experimental study of fasteners as a delamination arrest mechanism in composite laminates under mode I loading. Thin-Walled Structures 2023;191:111047.

[31] Carreras L, Renart J, Turon A, Costa J, Bak BLV, Lindgaard E, et al. A benchmark test for validating 3D simulation methods for delamination growth under quasi-static and fatigue loading. Compos Struct 2019;210:932–41.

[32] Carreras L, Bak BLV, Turon A, Renart J, Lindgaard E. Point-wise evaluation of the growth driving direction for arbitrarily shaped delamination fronts using cohesive elements. European Journal of Mechanics, A/Solids 2018;72:464–82.

[33] Benzeggagh ML, Kenane M. Measurement of mixed-mode delamination fracture toughness of unidirectional glass/epoxy composites with mixed-mode bending apparatus. Compos Sci Technol 1996;56:439–49.

[34] Carreras L, Lindgaard E, Renart J, Bak BLV, Turon A. An evaluation of mode-decomposed energy release rates for arbitrarily shaped delamination fronts using cohesive elements. Comput Methods Appl Mech Eng 2019;347:218–37.

[35] Carreras L, Bak BLV, Jensen SM, Lequesne C, Xiong H, Lindgaard E. Benchmark test for mode I fatigue-driven delamination in GFRP composite laminates: Experimental results and simulation with the inter-laminar damage model implemented in SAMCEF. Compos B Eng 2023;253.

[36] Turon A, Costa J, Camanho PP, Dávila CG. Simulation of delamination in composites under high-cycle fatigue. Compos Part A Appl Sci Manuf 2007;38:2270–82.

[37] Camanho PP, Dávila CG, De Moura MF. Numerical simulation of mixed-mode progressive delamination in composite materials. J Compos Mater 2003;37:1415–38.

[38] Harper PW, Hallett SR. A fatigue degradation law for cohesive interface elements - Development and application to composite materials. Int J Fatigue 2010;32:1774–87.

[39] Park S-J, Seo M-K. Solid-Solid Interfaces, 2011, p. 253–331.

[40] Kawashita LF, Hallett SR. A crack tip tracking algorithm for cohesive interface element analysis of fatigue delamination propagation in composite materials. Int J Solids Struct 2012;49:2898–913.

[41] Bak BLV, Turon A, Lindgaard E, Lund E. A benchmark study of simulation methods for high-cycle fatigue-driven delamination based on cohesive zone models. Compos Struct 2017;164:198–206.

[42] Rice JR. A Path Independent Integral and the Approximate Analysis of Strain Concentration by Notches and Cracks. J Appl Mech 1968;35:379–86.

[43] Bak BLV, Turon A, Lindgaard E, Lund E. A simulation method for high-cycle fatigue-driven delamination using a cohesive zone model. Int J Numer Methods Eng 2016;106:163–91.

[44] Harper PW, Hallett SR. Cohesive zone length in numerical simulations of composite delamination. Eng Fract Mech 2008;75:4774–92.

[45] Salvi LG, Bernasconi A, Martulli LM. Development of an automated remeshing simulation framework for quasi-static delamination propagation using the Virtual Crack Closure Technique. Under Review in Composites Part A: Applied Science and Manufacturing 2026.

[46] Martulli LM, Salvi L, Bernasconi A, Turon A, Carreras L. Numerical computations of the strain energy release rate for a comparative analysis of the virtual crack closure technique and a cohesive zone model and relative meshes. Mendeley Data, V1 2025.

[47] Yang Q, Cox B. Cohesive models for damage evolution in laminated composites. Int J Fract 2005;133:107–37.

[48] Mehrabi M, Martulli LM, Bernasconi A, Carboni M. Estimating crack tip position in adhesively bonded joints subjected to mode II quasi-static loading. Fatigue Fract Eng Mater Struct 2024;47:1262–80.

[49] Bogenfeld R, Freund S, Dähne S, Wunderlich T, Wille T. Damage tolerance allowable calculation for the aircraft design with static ultimate load. Compos Struct 2024;329:117803.

[50] Federal Aviation Administration. Advisory circular AC20-107B: Composites aircraft structure. U.S. Department of Transportation. 2009.

[51] Wu L, Tjahjanto D, Becker G, Makradi A, Jérusalem A, Noels L. A micro–meso-model of intra-laminar fracture in fiber-reinforced composites based on a discontinuous Galerkin/cohesive zone method. Eng Fract Mech 2013;104:162–83.

[52] Qin Y, Chen S, Asai M. Modeling of interfacial multi-cracks in dissimilar laminated structures using a nodal-based Lagrange multiplier/cohesive zone approach. Theoretical and Applied Fracture Mechanics 2024;133:104599.

Authors' accepted version. Engineering Fracture Mechanics, 112173 (2026).
https://doi.org/10.1016/j.engfracmech.2026.112173